SPRITE: 3-D SParse Radar Imaging TEchnique

Thomas Benoudiba-Campanini, Jean-François Giovannelli, and Pierre Minvielle

***Abstract*—An original 3-D high resolution radar imaging approach, called SPRITE for "SParse Radar Imaging TEchnique," is presented. It incorporates in an original way the available prior knowledge about the electromagnetic backscattering, extending the commonly used sparse point-wise scatterers to sparse facet-wise scatterers. It is based on a regularization scheme that accounts for information of sparsity and support. The radar map formation is performed efficiently based on a penalized and constrained criterion, and an Alternating Direction Method of Multipliers algorithm, largely used in image restoration and machine learning. It is customized in a such way that, at each iteration, the map update is fast in the frequency domain by 3-D FFT and IFFT while the updates of the auxiliary variables are direct and separable. SPRITE is both evaluated on synthetic and real measurement data from a spherical measurement setup. In comparison to the conventional method, called Polar Format Algorithm, the resolution is drastically enhanced. The main scatterers are recovered with increased accuracy, leading to a deeper understanding of the scattering behavior. Furthermore, compared to recent ℓ_1 based methods that are limited to point-wise scatterers, SPRITE and its facet-wise scatterers provide an impressive and improved spatial backscattering representation.**

***Index Terms*—3-D radar imaging, high resolution, inverse problem, sparse regularization, penalty, constraint, ADMM.**

I. Introduction

RADAR imaging, i.e. the map or image formation of the spatial distribution of reflectivity or backscattering, is often used for analysis purpose [1]. It helps to identify and characterize the radar reflective components of complex objects, with the aim to reduce the radar target signature (e.g. stealthy targets) or conversely to enhance it (e.g. corner reflectors on lifeboats). If one-dimensional (1D) backscattering profiles and two-dimensional (2D) backscattering maps have been widespread tools since the late 1970's, 3-D backscattering maps are far more complex to process. Indeed, 3-D radar imaging requires a time-consuming collection of the backscatter field data, i.e. an entire 2-D aperture, from which 3-D maps are formed. Conventional imaging methods, such as Polar Format Algorithm (PFA) or Filtered Backprojection (FBP) [1], are known to provide only moderate or even poor quality and resolution maps [1], [2].

To get high resolution (HR), it is essential to account for information and the paper introduces an idea of sparsity, meaning that the backscatter data can be explained with a low number of elements. Various methods had been proposed in the past. Let us mention the greedy algorithm CLEAN [3], [4] and the spectral methods, ESPRIT [5], [6] and MUSIC [7]–[9]. Notice that they do not deal with an image but rather with a set of point-wise elements. More recently, radar imaging has been considered as an inverse problem and solved by taking into account sparsity promoting priors [10]–[12]. In [13]–[17], radar imaging lies on the construction and optimization of a ℓ_1 penalized criterion. Similarly, a Bayesian strategy with a Laplacian prior law is applied in [18] to 2D Doppler radar imaging. Other works [13], [19] consist in sparse approaches that reconstruct simultaneously homogeneous areas and point-wise scatterers. It must be stressed that all the above mentioned methods lie on a model of point-wise scatterers. That turns out not to be completely coherent with the large range of wave-target interactions and specular reflections.

In this article, we propose an innovative sparsity promoting method for 3-D radar imaging. It is named SPRITE for "SParse Radar Imaging TEchnique". The SPRITE is based on a regularization approach resting on a ℓ_1-based penalized criterion that can include a support constraint. It tends to exhibit a limited number of plane facet-wise scatterers, possibly reduced to point-wise scatterers. It is consistent with a broader class of targets and wave-target interactions. The proposed constrained and convex non-differentiable criterion can be efficiently minimized by the primal-dual approach ADMM [20]. Based on an augmented Lagrangian procedure, it is specifically designed to take into account the specific problem structure. In the context of Radar Cross Section (RCS) analysis, i.e. radar signature analysis, applications to both simulated and real backscatter data show that the 3-D radar image resolution is drastically enhanced. Note that additional information can be found in [21] that presents the method for 1D backscattering profiles and in [22] that focuses on the radar data acquisition schema.

The article is organized as follows. In Section II the RCS data acquisition process is presented and the forward model is introduced. Section III is dedicated to the SPRITE where the estimated map is defined as the minimizer of a criterion including penalties and constraints. In Sections IV and V, results are respectively discussed for synthetic and real scattering measurements data. Finally, the conclusions are summarized in Section VI, including a few perspectives.

Manuscript received October 18, 2019; revised April 6, 2020; accepted May 17, 2020. Date of publication June 3, 2020; date of current version June 25, 2020. The associate editor coordinating the review of this manuscript and approving it for publication was Dr. Ilaria Catapano. *(Corresponding author: Thomas Benoudiba Campanini.)*

Thomas Benoudiba-Campanini is with the CEA CESTA, DAM, F-33114 Le Barp, France and also with the Groupe Signal-Image, IMS (Univ. Bordeaux - CNRS - BINP), F-33400 Talence, France (e-mail: thomas.benoudiba-campanini@cea.fr).

Jean-François Giovannelli is with the Groupe Signal-Image, IMS (Univ. Bordeaux - CNRS - BINP), F-33400 Talence, France (e-mail: giova@ims-bordeaux.fr).

Pierre Minvielle is with the CEA CESTA, DAM, F-33114 Le Barp, France (e-mail: pierre.minvielle@cea.fr).

Digital Object Identifier 10.1109/TCI.2020.2999162

II. Problem Formulation

A. RCS Data Acquisition

In standard RCS analysis, a monostatic radar illuminates an object with a quasi-planar monochromatic continuous wave (CW) of given frequency f and given wave vector $\boldsymbol{k}$ of magnitude k and unit direction $\hat{\boldsymbol{k}}$ (see [23] for details). The incident field is a vector $\boldsymbol{E}_i$ of complex amplitude E_i. The object backscatters a CW with the same frequency. The scattered field is a vector $\boldsymbol{E}_s$ of complex amplitude E_s. The complex scattering coefficient σ quantifies the object-wave interaction, including both amplitude and phase of the fields; it is linked with the RCS. Indeed, they can be defined in far field condition by:

$$\sigma = 2\sqrt{\pi}R\frac{E_s(R)}{E_i(R)};\ \text{RCS} = |\sigma|^2 \tag{1}$$

where R is the radar-object distance, large compared to the wavelength.

B. Forward Model

Let us introduce $a(\boldsymbol{r})$, also denoted $a(x, y, z)$, the spatial scattering distribution at the spatial position vector $\boldsymbol{r} = [x\ y\ z]^{\mathrm{t}}$ in the spatial coordinate space $(O\,\hat{\boldsymbol{x}}\,\hat{\boldsymbol{y}}\,\hat{\boldsymbol{z}})$. It does not depend on $\boldsymbol{k}$ in a "small angle small bandwidth" context [24] where the variations of $\boldsymbol{k}$ are small enough around $\boldsymbol{k}_c$, a central wave vector of interest. The classical forward model derives from optical physics and stationary-phase approximation in high frequency [25]. It is given by:

$$\sigma(\boldsymbol{k}) = \iiint_{\mathcal{D}} a(\boldsymbol{r}) \exp\left[-2\jmath\pi\boldsymbol{k}\cdot\boldsymbol{r}\right] \mathrm{d}\,\boldsymbol{r}, \tag{2}$$

where $\mathcal{D}$ is the field-of-view. Note that it also derives from the Born approximation which is more suitable for problems involving semi-transparent targets and long wavelengths [26]. Nevertheless, such a model leaves out various physical phenomena: multiple scattering, creeping waves, shadowing, etc. Yet, it is extensively used because it makes the observation model linear, at the cost of possible artifacts in the reconstructed scattering map [27].

The complex scattering coefficient σ can be measured with an appropriate instrumentation system (antenna, network analyzer, etc.) and a calibration process. Let us collect M measured scattering coefficients, for M wave vectors $\boldsymbol{k}_1, \boldsymbol{k}_2, \ldots, \boldsymbol{k}_M$. Otherwise, let us discretize the spatial scattering distribution into N voxels ($N = N_x N_y N_z$ where N_x, N_y and N_z are respectively along the $\hat{\boldsymbol{x}}$, $\hat{\boldsymbol{y}}$ and $\hat{\boldsymbol{z}}$ axis). Then, model (2) leads to the discretized linear observation model:

$$\boldsymbol{\sigma} = \boldsymbol{H}\boldsymbol{a} + \boldsymbol{n} \tag{3}$$

where $\boldsymbol{\sigma} \in \mathbb{C}^M$ is the observation vector, $\boldsymbol{a} \in \mathbb{C}^N$ the vectorized scattering map, $\boldsymbol{n} \in \mathbb{C}^M$ the noise vector accounting for model and measurement errors, and $\boldsymbol{H} \in \mathbb{C}^{M\times N}$ the model matrix. Note that this linear model is classical and appears in many other domains (see for example [28], [29]).

If the acquisition wave vectors $\boldsymbol{k}_1, \boldsymbol{k}_2, \ldots, \boldsymbol{k}_M$ lie on a k-space Cartesian grid it can be shown that $\boldsymbol{H}$ can be expressed as (see proof in appendix A):

$$\boldsymbol{H} = \alpha\sqrt{N}\,\boldsymbol{\Delta}_\Psi \boldsymbol{S}\boldsymbol{F}\boldsymbol{\Delta}_\Phi \tag{4}$$

where $\alpha \in \mathbb{C}$ is a complex coefficient accounting for the origin phase difference of the spatial and the k-space grids, $\boldsymbol{S} \in \mathbb{R}^{M\times N}$ is a 0/1-binary selection (or sampling) matrix ($\boldsymbol{S}$ discards unobserved spatial frequencies), $\boldsymbol{F} \in \mathbb{C}^{N\times N}$ is an unitary 3-D discrete Fourier transform matrix, $\boldsymbol{\Delta}_\Psi \in \mathbb{C}^{M\times M}$ and $\boldsymbol{\Delta}_\Phi \in \mathbb{C}^{N\times N}$ are diagonal phase shifting matrices, respectively in the k-space and in the spatial domain. As it is, eq. (4) involves a discrete Fourier transform on a Cartesian grid, so it can be computed in a very efficient way by FFT.

In order to take advantage of this crucial efficiency, a standard step is to include a regridding process. Note that we use an *incomplete nearest neighbor* regridding process (see description in appendix B). This method consists in examining the acquisition grid, rather than the Cartesian grid with other interpolation methods, and assigning each measure from the acquisition grid to the closest point of the Cartesian grid. Let us stress that this method does not require the problematic addition of synthetic data: it does not affect value where there is no measurement and it does not force the unobserved coefficients to zero nor another value. At some point, a part of the resolution improvement also results from this particular reggriding.

C. Inverse Problem

Considering the linear observation model (4), the goal is to determine the scattering map $\boldsymbol{a}$ from the observed vector $\boldsymbol{\sigma}$ from (3). In this way, it is clearly an inverse problem [29]. Then, it must be stressed that $\boldsymbol{H}$ is and not invertible since $N \gg M$, i.e. the number of unknowns is far larger than the data dimension. It is then mandatory to regularize the problem. In one way or another, that involves incorporating prior information on the unknown scattering map $\boldsymbol{a}$ [28], [30].

That is how conventional methods work more or less explicitly. Thus, standard Polar Format Algorithm (PFA) [1], [24] turns out to be equivalent to the minimum-norm least-squares solution when the observations are arranged on a Cartesian grid [23]. On one hand, the image resolution is limited by the frequency bandwidth for the range resolution and on the other hand by the angular diversity of observations and the wavelength for the cross-range resolution [1]. Moreover, according to the Fourier theory, the finite bandwidth of the radar leads to a particular point spread function: a cardinal sine defocusing function around the scattering centers. This is particularly problematic in RCS analysis because low scatterers may be hidden by a high sidelobe. Many methods, mainly based on a spectral weighting called apodization, had been studied in the past to enhance the Peak to SideLobe Ratio (PSLR). However, even if the PSLR is significantly improved, the main lobe beamwidth is increased at the same time, leading to a degraded resolution.

More recently, [13]–[17] have proposed sparse regularization methods for RCS imaging. They rest on the minimization of a criterion with a least square term and a sparse promoting penalty such as the ℓ_1 norm of the scattering map. The results are similar to those that can by obtained with greedy algorithms such as

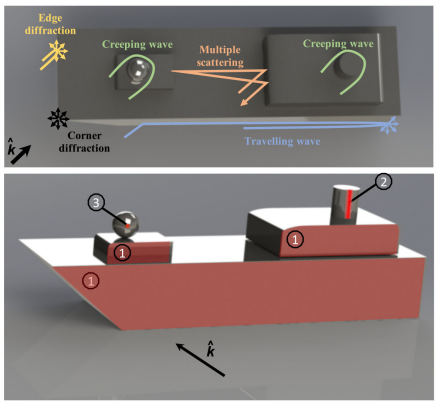

Fig. 1. Various electromagnetic interactions ($\hat{\boldsymbol{k}}$: wave vector direction). From facet specular scattering (1), segment scattering (2) and point-wise scattering (3) to more complex phenomena (above).

CLEAN [3], [4] and Orthogonal Matching Pursuit methods [17], as well as spectral estimation methods such as ESPRIT [5], [6] and MUSIC [7], [9]. In all cases, the estimated map is made up of scattering points. And yet, it is well known that in a high frequency context, specular reflections are the main scattering mechanisms [31]. Thus, the 3-D map should not only be composed of scattering points but also of scattering segments and flat surfaces also called specular (plane) facets [32]. See Fig. 1 for a quick recap on electromagnetic scattering phenomena. They account for diffractions and specular reflections with local plane surface orthogonal to the wave vector. The proposed SPRITE, by reformulating sparsity, provides an efficient way to take into account these various wave-object interactions, leading to high quality and resolution images.

III. The SPRITE

A. Backscattering Prior Knowledge

Let us make the radar imaging context more precise. A monostatic radar illuminates an object whose surface is smooth relatively to the radar wavelength. Again, we consider a high frequency situation where physical optics and the forward model (2) apply. Moreover, let us mention that the $\hat{\boldsymbol{z}}$ axis is chosen to be collinear to the central wave vector $\boldsymbol{k}_c$.

In this context, even before getting the measurements, it is possible to formulate a comprehensive knowledge about the backscattering that returns to the radar. It can be expressed through the five following priors on the 3-D map $\boldsymbol{a}$.

1) *Sparsity:* as illustrated in Fig. 2, there is a small number of planes $\mathcal{P}$ tangent to the target surface and orthogonal to $\boldsymbol{k}_c$. By definition, only these planes contain scattering points, scattering segments and specular facets. Thereby, as shown in Fig. 3, for $n_z = 0, \dots N_z - 1$ the projection $P(n_z)$ of $\boldsymbol{a}$ onto $\hat{\boldsymbol{z}}$ is sparse:

$$P(n_z) = \sum_{n_x=0}^{N_x-1} \sum_{n_y=0}^{N_y-1} \boldsymbol{a}_{n_x,n_y,n_z}$$

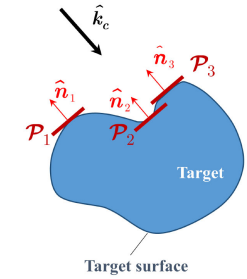

Fig. 2. Planes tangent to the target surface and orthogonal to $\hat{\boldsymbol{k}}_c$

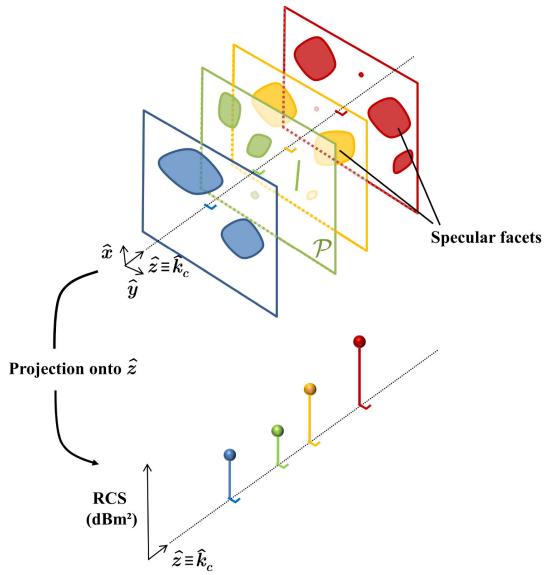

Fig. 3. Specular plane facets and projection of $\boldsymbol{a}$ onto $\hat{\boldsymbol{z}}$.

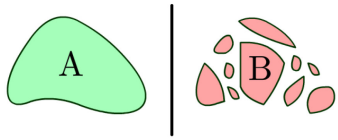

Fig. 4. $\boldsymbol{a}$ is made up of a small number of connected facets (A) rather than many unconnected facets (B).

2) *Compactness:* as the target surface is smooth relative to the wavelength, the map $\boldsymbol{a}$ is made up of a small number of specular facets which are connected in a topological sense (see Fig. 4).
3) *Piecewise constant:* the scattering coefficient is constant all over each facet [31]. Thus, the map $\boldsymbol{a}$ is piecewise constant. Indeed, the backscattering is supposed to come from a homogeneous part of the locally smooth object or from a local material interface where the material properties are invariant, and so the proper amplitude and phase do not vary on the specular facet.
4) *Low energy:* the map energy

$$E = \sum_{n_x=0}^{N_x-1} \sum_{n_y=0}^{N_y-1} \sum_{n_z=0}^{N_z-1} |\boldsymbol{a}_{n_x,n_y,n_z}|^2$$

is low. This assumption is particularly true for stealth targets [23]. Moreover, this prior promotes "non-explosive" maps because it enforces smoothness by improving the conditioning of the problem.

5) *Limited support:* the electromagnetic extent of the target lies in a finite spatial support outside the reflectivity is assumed to be 0, as explained in [33]. Notice that this prior can be loosen : if no prior information on the support is available, the chosen support should be the whole space.

B. Criterion, Penalties and Constraint

From now on, the approach consists in constructing a criterion for which the estimated scattering map $\hat{\boldsymbol{a}}$ is the minimizer. Firstly, it requires to take into account the coherence with the observed data $\boldsymbol{\sigma}$. Secondly, for regularization purpose, it is appropriate to incorporate the previously detailed priors. With this aim, we propose an approach based on a penalized and constrained criterion.

Let us start by expressing each prior with an associated penalty term that will favour coherent solutions.

- Prior 1) results in a $\|\boldsymbol{P}\boldsymbol{a}\|_1$ penalty where $\boldsymbol{P}$ is a projection matrix onto $\hat{\boldsymbol{z}}$.
- Priors 2) and 3) lead to $\|\boldsymbol{D}_x\boldsymbol{a}\|_1$ and $\|\boldsymbol{D}_y\boldsymbol{a}\|_1$ penalties, where $\boldsymbol{D}_x$ and $\boldsymbol{D}_y$ are the pixel-wise difference matrices along the $\hat{\boldsymbol{x}}$ and $\hat{\boldsymbol{y}}$ axis. Note that they correspond to an anisotropic total variation [34] along the $\hat{\boldsymbol{x}}$ and $\hat{\boldsymbol{y}}$ axis. Furthermore, a circulant approximation is made to these 3-level Tœplitz matrices in order to reduce the computational cost [35]. Note that this approximation is valid when the object is centered within a large enough field-of-view (see [36] for details about the matrices structure).
- Prior 4) result in a $\|\boldsymbol{a}\|_2^2$ penalty. It also ensure the strict convexity of the further criterion and then the uniqueness of the solution.
- Prior 5) is not expressed by a penalty but by a constraint set $\mathcal{C}$.

Consequently, let us introduce the following criterion:

$$\begin{aligned}\mathcal{J}(\boldsymbol{a}) = &\frac{1}{2}\|\boldsymbol{\sigma}-\boldsymbol{H}\boldsymbol{a}\|_2^2 + \mu\|\boldsymbol{P}\boldsymbol{a}\|_1 \\ &+ \lambda\|\boldsymbol{D}_x\boldsymbol{a}\|_1 + \lambda\|\boldsymbol{D}_y\boldsymbol{a}\|_1 + \frac{\nu}{2}\|\boldsymbol{a}\|_2^2\end{aligned} \tag{5}$$

where $\|\boldsymbol{\sigma}-\boldsymbol{H}\boldsymbol{a}\|_2^2$ is the data fitting term and μ, λ and ν are positive regularization parameters. They control the trade-off between the data fitting term and the penalties and so they affect $\mathcal{J}(\boldsymbol{a})$ and finally the estimated map. Finally, the estimated map $\hat{\boldsymbol{a}}$ is defined as :

$$\hat{\boldsymbol{a}} = \underset{\boldsymbol{a}\in\mathbb{C}^N}{\operatorname{argmin}} \begin{cases} \mathcal{J}(\boldsymbol{a}) \\ \text{s.t. } \boldsymbol{a}\in\mathcal{C} \end{cases} \tag{6}$$

where $\mathcal{C}$ is a closed convex constraint set [20]. Admittedly the criterion (5) is convex, but ℓ_1 norms make it non-differentiable. Moreover, when $\nu > 0$, the criterion is strictly convex. This ensures the existence and uniqueness of the solution (6) (see [37] for the proof).

C. Convex Non-Differentiable Optimization

First of all, let us emphasize that this high-dimensional optimization problem (6) is tricky. This notwithstanding, there is a vast literature devoted to non-differentiable convex minimization. For instance, we can cite:

- ℓ_1 smoothing methods [38] (e.g. the ℓ_1 norm is replaced by a differentiable Huber function),
- subgradient methods [39],
- proximal gradient methods such as the Forward Backward Splitting [40], [41] with its accelerated version the Fast Iterative Thresholding Algorithm [42],
- primal-dual methods such as the dual ascent method, the method of Lagrange multipliers and the Alternating Direction Method of Multipliers (ADMM) [20] (see also [43] and [44]).

The ADMM method belongs to the convex optimization algorithms class. It is based on an augmented Lagrangian approach and is very suitable to find the constrained solution (6). Moreover, in our case, the convergence is known to be guaranteed because $\mathcal{J}(\boldsymbol{a})$ is strictly convex for $\nu > 0$ [45]. In an ADMM form, the optimization problem (6) can be reformulated by:

$$\hat{\boldsymbol{a}} = \underset{\boldsymbol{a},\boldsymbol{v}}{\operatorname{argmin}} \begin{cases} \mathcal{K}(\boldsymbol{a},\boldsymbol{v}) \\ \text{s.t. } \begin{cases} \boldsymbol{v}_P = \boldsymbol{P}\boldsymbol{a} \\ \boldsymbol{v}_x = \boldsymbol{D}_x\boldsymbol{a} \\ \boldsymbol{v}_y = \boldsymbol{D}_y\boldsymbol{a} \\ \boldsymbol{v}_{\mathcal{C}} = \boldsymbol{a} \end{cases} \end{cases} \tag{7}$$

where

$$\begin{aligned}\mathcal{K}(\boldsymbol{a},\boldsymbol{v}) = &\frac{1}{2}\|\boldsymbol{\sigma}-\boldsymbol{H}\boldsymbol{a}\|_2^2 + \mu\|\boldsymbol{v}_P\|_1 + \lambda\|\boldsymbol{v}_x\|_1 \\ &+ \lambda\|\boldsymbol{v}_y\|_1 + \frac{\nu}{2}\|\boldsymbol{a}\|_2^2 + \mathcal{I}_{\mathcal{C}}(\boldsymbol{v}_{\mathcal{C}})\end{aligned}$$

and with $\boldsymbol{v} = [\boldsymbol{v}_P, \boldsymbol{v}_x, \boldsymbol{v}_y, \boldsymbol{v}_{\mathcal{C}}]$ the vector of auxiliary variables and $\mathcal{I}_{\mathcal{C}}$ the characteristic function of $\mathcal{C}$:

$$\mathcal{I}_{\mathcal{C}}(v) = \begin{cases} 0, & \text{if } v\in\mathcal{C} \\ +\infty & \text{otherwise} \end{cases}.$$

Note that the solutions (6) and (7) are strictly equal: indeed, for any couple $(\bar{\boldsymbol{a}},\bar{\boldsymbol{v}})$ that meets the constraints of (7), we have $\mathcal{K}(\bar{\boldsymbol{a}},\bar{\boldsymbol{v}}) = \mathcal{J}(\bar{\boldsymbol{a}})$ and $\bar{\boldsymbol{a}}\in\mathcal{C}$ so, minimisation of $\mathcal{J}(\boldsymbol{a})$ w.r.t. $\boldsymbol{a}$ s.t. $\boldsymbol{a}\in\mathcal{C}$ amounts to minimisation of $\mathcal{K}(\boldsymbol{a},\boldsymbol{v})$ w.r.t. $(\boldsymbol{a},\boldsymbol{v})$.

Let us now introduce the Lagrangian function of the problem (7). For numerical efficiency we consider the augmented Lagrangian function and for notational convenience the so-called version is preferred [45], [46]:

$$\begin{aligned}\mathcal{L}(\boldsymbol{a},\boldsymbol{v},\boldsymbol{u}) = \mathcal{K}(\boldsymbol{a},\boldsymbol{v}) &+ \frac{\rho_{\mathcal{C}}}{2}\left(\|\boldsymbol{a}-\boldsymbol{v}_{\mathcal{C}}+\boldsymbol{u}_{\mathcal{C}}\|_2^2 - \|\boldsymbol{u}_{\mathcal{C}}\|_2^2\right) \\ &+ \frac{\rho_P}{2}\left(\|\boldsymbol{P}\boldsymbol{a}-\boldsymbol{v}_P+\boldsymbol{u}_P\|_2^2 - \|\boldsymbol{u}_P\|_2^2\right) \\ &+ \frac{\rho_D}{2}\Big(\|\boldsymbol{D}_x\boldsymbol{a}-\boldsymbol{v}_x+\boldsymbol{u}_x\|_2^2 - \|\boldsymbol{u}_x\|_2^2 \\ &+ \|\boldsymbol{D}_y\boldsymbol{a}-\boldsymbol{v}_y+\boldsymbol{u}_y\|_2^2 - \|\boldsymbol{u}_y\|_2^2\Big)\end{aligned} \tag{8}$$

where $\boldsymbol{u} = [\boldsymbol{u}_P, \boldsymbol{u}_x, \boldsymbol{u}_y, \boldsymbol{u}_{\mathcal{C}}]$ is the vector of the scaled Lagrange multipliers and $\boldsymbol{\rho} = [\rho_P, \rho_D, \rho_{\mathcal{C}}]$ is the vector of the strictly

Initialize $\boldsymbol{v}^{(0)}$, $\boldsymbol{u}^{(0)}$ and $k=0$.
begin

$$\boldsymbol{a}^{(k+1)} = \underset{\boldsymbol{a}}{\operatorname{argmin}}\, \mathcal{L}(\boldsymbol{a}, \boldsymbol{v}^{(k)}, \boldsymbol{u}^{(k)})$$
$$\boldsymbol{v}_P^{(k+1)} = \underset{\boldsymbol{v}_P}{\operatorname{argmin}}\, \mathcal{L}(\boldsymbol{a}^{(k+1)}, \boldsymbol{v}_P, \boldsymbol{v}_x^{(k)}, \boldsymbol{v}_y^{(k)}, \boldsymbol{v}_{\mathcal{C}}^{(k)}, \boldsymbol{u}^{(k)})$$
$$\boldsymbol{v}_x^{(k+1)} = \underset{\boldsymbol{v}_x}{\operatorname{argmin}}\, \mathcal{L}(\boldsymbol{a}^{(k+1)}, \boldsymbol{v}_P^{(k+1)}, \boldsymbol{v}_x, \boldsymbol{v}_y^{(k)}, \boldsymbol{v}_{\mathcal{C}}^{(k)}, \boldsymbol{u}^{(k)})$$
$$\boldsymbol{v}_y^{(k+1)} = \underset{\boldsymbol{v}_y}{\operatorname{argmin}}\, \mathcal{L}(\boldsymbol{a}^{(k+1)}, \boldsymbol{v}_P^{(k+1)}, \boldsymbol{v}_x^{(k+1)}, \boldsymbol{v}_y, \boldsymbol{v}_{\mathcal{C}}^{(k)}, \boldsymbol{u}^{(k)})$$
$$\boldsymbol{v}_{\mathcal{C}}^{(k+1)} = \underset{\boldsymbol{v}_{\mathcal{C}}}{\operatorname{argmin}}\, \mathcal{L}(\boldsymbol{a}^{(k+1)}, \boldsymbol{v}_P^{(k+1)}, \boldsymbol{v}_x^{(k+1)}, \boldsymbol{v}_y^{(k+1)}, \boldsymbol{v}_{\mathcal{C}}, \boldsymbol{u}^{(k)})$$
$$\boldsymbol{u}_P^{(k+1)} = \boldsymbol{u}_P^{(k)} + \boldsymbol{P}\boldsymbol{a}^{(k+1)} - \boldsymbol{v}_P^{(k+1)}$$
$$\boldsymbol{u}_x^{(k+1)} = \boldsymbol{u}_x^{(k)} + \boldsymbol{D}_x\boldsymbol{a}^{(k+1)} - \boldsymbol{v}_x^{(k+1)}$$
$$\boldsymbol{u}_y^{(k+1)} = \boldsymbol{u}_y^{(k)} + \boldsymbol{D}_y\boldsymbol{a}^{(k+1)} - \boldsymbol{v}_y^{(k+1)}$$
$$\boldsymbol{u}_{\mathcal{C}}^{(k+1)} = \boldsymbol{u}_{\mathcal{C}}^{(k)} + \boldsymbol{a}^{(k+1)} - \boldsymbol{v}_{\mathcal{C}}^{(k+1)}$$
$$k = k+1$$

positive constant penalty parameters. Note that, contrary to the regularization parameters, the penalty parameters do not affect the solution: indeed, when the constraints are met $\mathcal{L}(\boldsymbol{a}, \boldsymbol{v}, \boldsymbol{u}) = \mathcal{K}(\boldsymbol{a}, \boldsymbol{v})$. As a consequence, they only drive the convergence rate [45]. Let us stress that the Lagrangian formulation is proved to be suitable to solve such a problem problem because (8) is quadratic, strictly convex and differentiable with respect to $\boldsymbol{a}$ (see proof in appendix C) and separable with respect to the other variables.

The pseudo-code of the SPRITE algorithm is detailed below.

It is an iterative algorithm that alternates updates of the map $\boldsymbol{a}$ and of the auxiliary variables $\boldsymbol{v}$ and $\boldsymbol{u}$. Let us examine in detail these updates.

- *The $\boldsymbol{a}$-update* is obtained by nullifying the gradient of (8) (see proof in appendix C). That leads to:

$$\boldsymbol{a}^{(k+1)} = \boldsymbol{G}^{-1}\boldsymbol{d}^{(k)} \tag{9}$$

where $\boldsymbol{d}^{(k)} = \boldsymbol{H}^{\dagger}\boldsymbol{\sigma} + \boldsymbol{t}^{(k)}$ with

$$\boldsymbol{t}^{(k)} = \rho_P\boldsymbol{P}^{\dagger}(\boldsymbol{v}_P^{(k)} - \boldsymbol{u}_P^{(k)}) + \rho_{\mathcal{C}}(\boldsymbol{v}_{\mathcal{C}}^{(k)} - \boldsymbol{u}_{\mathcal{C}}^{(k)}) + \rho_D\left[\boldsymbol{D}_x^{\dagger}(\boldsymbol{v}_x^{(k)} - \boldsymbol{u}_x^{(k)}) + \boldsymbol{D}_y^{\dagger}(\boldsymbol{v}_y^{(k)} - \boldsymbol{u}_y^{(k)})\right],$$

where $\dagger$ denotes the Hermitian transpose and $\boldsymbol{G} = \boldsymbol{H}^{\dagger}\boldsymbol{H} + \rho_P\boldsymbol{P}^{\dagger}\boldsymbol{P} + \rho_D(\boldsymbol{D}_x^{\dagger}\boldsymbol{D}_x + \boldsymbol{D}_y^{\dagger}\boldsymbol{D}_y) + (\nu + \rho_{\mathcal{C}})\boldsymbol{I}_N$. It must be noted that $\boldsymbol{H}^{\dagger}\boldsymbol{H}, \boldsymbol{P}^{\dagger}\boldsymbol{P}, \boldsymbol{D}_x^{\dagger}\boldsymbol{D}_x, \boldsymbol{D}_y^{\dagger}\boldsymbol{D}_y$ and $\boldsymbol{I}_N$ are in relation with linear shift-invariant filters, more specifically circular shift invariant[1] so these matrices are 3-level circulant matrices (proofs are given in [36], pp. 173–182). Thus, $\boldsymbol{G}$ is also a 3-level circulant matrix which can be diagonalized in the Fourier domain (see [47], [48]): $\boldsymbol{G} = \boldsymbol{F}^{\dagger}\boldsymbol{\Lambda}_{\boldsymbol{G}}\boldsymbol{F}$. It follows that the $\boldsymbol{a}$-update can be computed quickly by using 3-D FFT and IFFT:

$$\boldsymbol{a}^{(k+1)} = \alpha N\boldsymbol{F}^{\dagger}\boldsymbol{\Lambda}_{\boldsymbol{G}}^{-1}\boldsymbol{F}(\boldsymbol{\Delta}_{\Phi}^{\dagger}\boldsymbol{F}^{\dagger}\boldsymbol{S}^t\boldsymbol{\Delta}_{\Psi}^{\dagger}\boldsymbol{\sigma} + \boldsymbol{t}^{(k)}) \tag{10}$$

[1]Rigorously, $\boldsymbol{D}_x$ and $\boldsymbol{D}_y$ are basically shift-invariant and not circular shift invariant but they are approximated as circular shift invariant. The approximation is valid since the object is in the center of the field of view.

TABLE I
SYNTHETIC MAP FACETS

Facet	**C**	**E**	**A**
Longitudinal position (m)	$-0,21$	0	$0,20$
Amplitude (dB)	-40	-45	-50
Phase shift (rad)	$\pi/4$	$\pi/2$	$\pi/3$

Note that $\boldsymbol{\Delta}_{\Phi}^{\dagger}\boldsymbol{F}^{\dagger}\boldsymbol{S}^t\boldsymbol{\Delta}_{\Psi}^{\dagger}\boldsymbol{\sigma}$ is basically the PFA map; it can be precomputed efficiently with 3-D FFT and IFFT.

- *The $\boldsymbol{v}$-update* can be written (see proof in appendix D):

$$\begin{aligned}
\boldsymbol{v}_P^{(k+1)} &= \mathrm{S}_{\mu/\rho_P}\left(\boldsymbol{P}\boldsymbol{a}^{(k+1)} + \boldsymbol{u}_P^{(k)}\right)\\
\boldsymbol{v}_x^{(k+1)} &= \mathrm{S}_{\lambda/\rho_D}\left(\boldsymbol{D}_x\boldsymbol{a}^{(k+1)} + \boldsymbol{u}_x^{(k)}\right)\\
\boldsymbol{v}_y^{(k+1)} &= \mathrm{S}_{\lambda/\rho_D}\left(\boldsymbol{D}_y\boldsymbol{a}^{(k+1)} + \boldsymbol{u}_y^{(k)}\right)\\
\boldsymbol{v}_{\mathcal{C}}^{(k+1)} &= \mathcal{P}_{\mathcal{C}}(\boldsymbol{a}^{(k+1)} + \boldsymbol{u}_{\mathcal{C}}^{(k)})
\end{aligned} \tag{11}$$

where $\mathcal{P}_{\mathcal{C}}$ is the Euclidean projection onto $\mathcal{C}$ and S the soft thresholding operator for complex variables [46]:

$$\mathrm{S}_{\lambda}(\boldsymbol{v}) = \frac{\max\{|\boldsymbol{v}| - \lambda, 0\}}{\max\{|\boldsymbol{v}| - \lambda, 0\} + \lambda}\,\boldsymbol{v} \tag{12}$$

and it also known as the proximity operator of the ℓ_1 norm. Let us emphasize that the $\boldsymbol{v}$ and $\boldsymbol{u}$ updates are direct and separable.

On the whole, let us stress that the non-quadratic, non-differentiable and constraint problem (7) is solved very efficiently by the ADMM. More specifically, the latter alternates updates that requires a large system solver but computable by FFT and IFFT (see (11)) and updates that are separable, so computed in parallel (see (10). Moreover, let us emphasize that due to the strict convexity of the criterion (5), the ADMM is known to converge towards Green $\underline{a}$ the unique solution $\hat{\boldsymbol{a}}$.

IV. VALIDATION ON SYNTHETIC DATA

The SPRITE is first validated on synthetic data. Let us consider a map with three specular facets forming the letters "**C**," "**E**" and "**A**"; the normals are collinear to the central wave vector $\boldsymbol{k}_c$. The longitudinal position, the amplitude and the phase shift of each facet are detailed in Table I. Fig. 5(a) provides a 3-D representation of this synthetic map as well as a longitudinal cut along $(\hat{\boldsymbol{x}}\hat{\boldsymbol{z}})$.

Data are simulated with the observation model (3) for wave frequencies varying from 8 to 12 GHz with increments of 5 MHz and angle variation $\theta = [-15^{\circ} : 1^{\circ} : 15^{\circ}]$ and $\varphi = [-15^{\circ} : 1^{\circ} : 15^{\circ}]$. A white Gaussian noise is added to the data and the SNR is $-7,7$ dB.

The RCS map is computed on a grid with $N = 10^6$ voxels ($N_x \times N_y \times N_z = 100 \times 100 \times 100$). In Fig. 5, the SPRITE is compared to the conventional PFA and to ℓ_1 norm penalization method [13], [15]–[17]. The regularization parameters are manually tuned: $\mu = 10, \lambda = 100, \nu = 150$.

In comparison to the PFA map, the resolution is drastically increased with the proposed SPRITE. The facets are perfectly

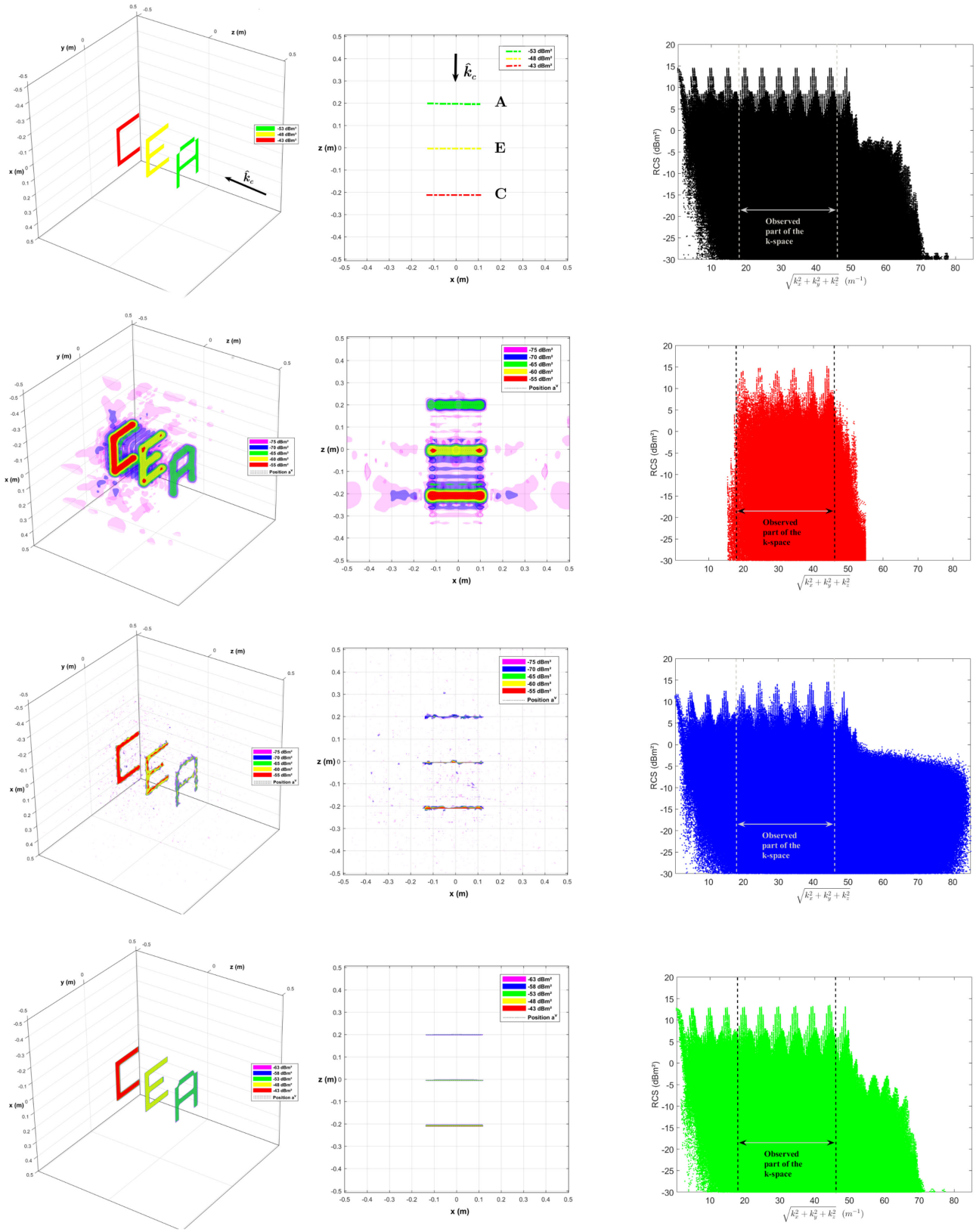

Fig. 5. 3-D RCS maps. First two columns: spatial representation. Third column: spectral representation. From top to bottom: Synthetic map, PFA, ℓ_1 norm regularization [16] ($\mu = 0,01$), SPRITE.

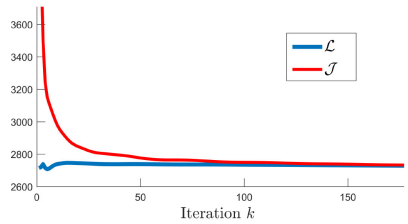

Fig. 6. Criterion and Lagrangian functions versus iterations.

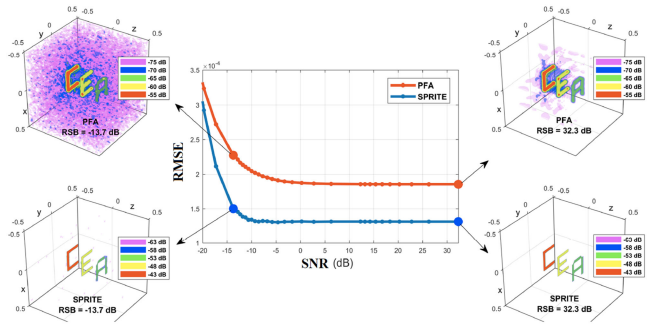

Fig. 7. Comparison of the PFA and the SPRITE RMSE for different SNR.

located and their amplitude and phase well estimated. Moreover, as the SPRITE takes into account the possible presence of specular facets, the resolution of the reconstructed map is better than the one estimated with the ℓ_1 penalization method which only promotes scattering points.

In the right column of Fig. 5, the k-space contents of the maps are compared. The x-axis is the distance from the origin of the k-space and the y-axis is the RCS. The observed part of the k-space is represented between the dashed vertical lines. It can be noticed that contrary to the PFA, the SPRITE correctly completes the k-space outside of the observed part. Moreover, the ℓ_1 method overestimates the low and high spatial-frequencies. This can be explained because the ℓ_1 map is made of scattering points, that is a sum of Dirac functions, whose spectral content is constant.

The augmented Lagrangian and the criterion evolutions are represented in Fig. 6. It can be seen that the algorithm converges in a hundred of iterations. The convergence time is 3 min 49 sec.[2] It must be noticed that ADMM is not a decreasing algorithm concerning the Lagrangian and the criterion. Indeed, the criterion is not monotonically decreasing but it asymptotically converges towards its minimum. The Lagrangian converges towards its saddle point value.

A robustness analysis on noise-corrupted data is made for both the PFA and the SPRITE. Again, as it is a commonly assumed in radar measurement [1], [49], an additive white Gaussian noise is considered. The root-mean-square error: $\text{RMSE} = \|\hat{\boldsymbol{a}}_{\mathcal{M}} - \boldsymbol{a}^s\|_2/\sqrt{N}$ is used to quantify the estimation error of each method, where $\hat{\boldsymbol{a}}_{\mathcal{M}}$ is the estimated map according to the method $\mathcal{M}$ and $\boldsymbol{a}^s$ is the synthetic map. In Fig. 7, the evolution of the RMSE of $\hat{\boldsymbol{a}}_{\text{PFA}}$ and $\hat{\boldsymbol{a}}_{\text{SPRITE}}$ for different SNR values are compared. It can be seen that the SPRITE is much more robust to a white Gaussian noise than the PFA and it supports low SNR.

[2]MATLAB 2013b, Intel Xeon E5-2620 v3 2.4 GHz, 32 GB RAM

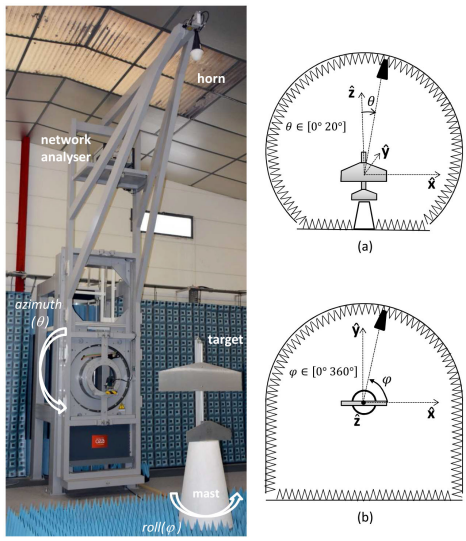

Fig. 8. Spherical measurement setup.

V. Applications to Real Data

A. Spherical Measurement Setup

The method is evaluated on real measurements from the spherical setup of Fig. 8. The microwave instrumentation is made up of two bipolarization monostatic radio frequency (RF) transmitting and receiving antennas, a wideband standard gain horn equipped with a lens, that are driven by a fast network analyzer. A θ rotation is achieved using a direct drive positioner including a brushless motor. The φ rotation uses another positioner. The polystyrene mast supporting the target under test is located on this rotation positioning system. See [23] for further details. Consequently, for a given frequency f, roll angle φ and elevation angle θ (obtained by rotating both antenna and target), the wave vector $\boldsymbol{k}$ is expressed by:

$$\boldsymbol{k} = -\frac{2\pi f}{c}\begin{bmatrix}\sin(\theta)\cos(\varphi)\\ \sin(\theta)\sin(\varphi)\\ \cos(\theta)\end{bmatrix}$$

where c is the light speed.

The measurement procedure consists of successive steps. Firstly, a calibration by substitution [31] is performed with a standard target (300 mm diameter PEC metallic sphere) whose RCS is computed by Mie series. Secondly, a background subtraction [31] is operated in order to eliminate the background echoes. It is commonly used when the clutter is higher than the target under test. Finally, an adaptive range filter is applied to remove the residual stray echoes that could affect the useful signal (e.g. interactions with walls and floor). Scattering measurements are made for wave frequencies varying from 8 to 12 GHz with increments of 3.9 MHz and angle variation $\theta = [-20° : 1° : 20°]$ and $\varphi = [-20° : 4° : 20°]$.

B. RCS Analysis

The target is a metallic Perfectly Electrically Conducting (PEC) right circular cone [21] (height: 598.47 mm, base

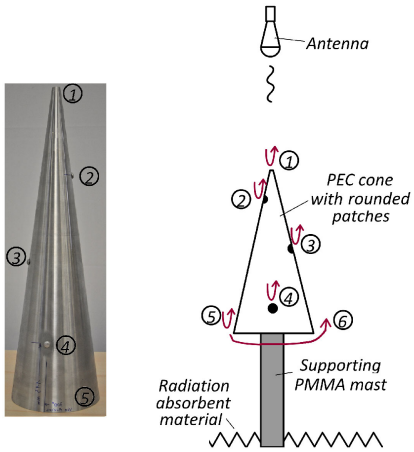

Fig. 9. PEC cone (left) and backscattered echoes (right).

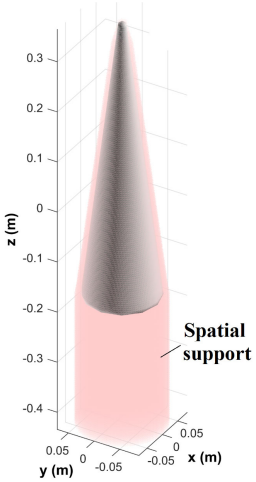

Fig. 10. Spatial support constraint.

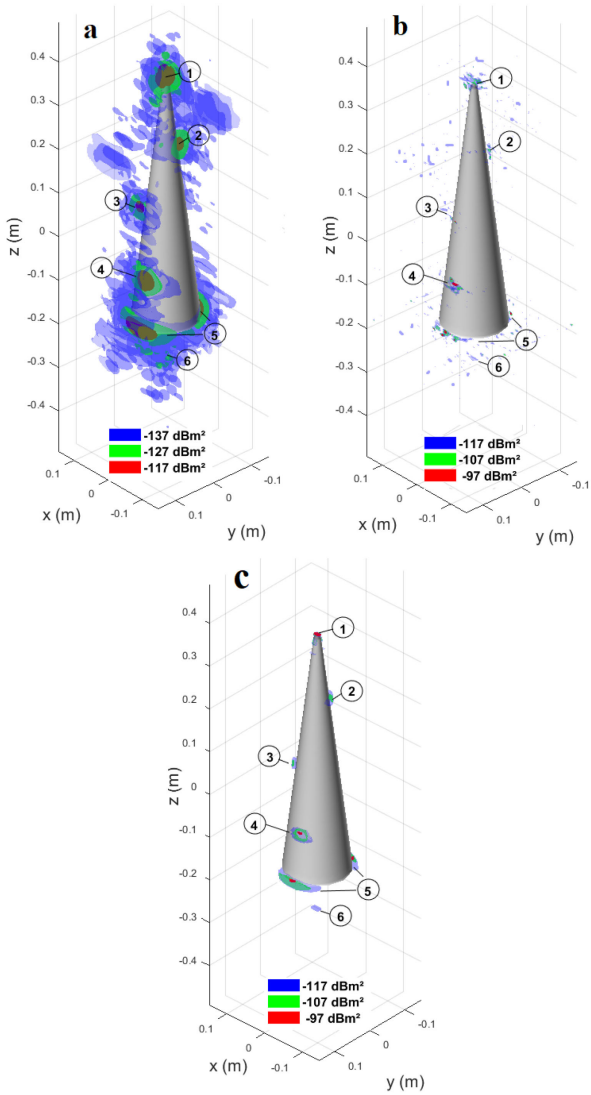

Fig. 11. 3-D RCS estimated maps with: a) PFA – b) ℓ_1 norm regularization [13], [15]–[17] – c) SPRITE. *For a better RCS analysis purpose the target shape is displayed.*

diameter: 149.33 mm, aperture: $14.22°$) of Fig. 9, where 3 metallic rounded patches have been glued to points ② z = 115 mm ($270°$ roll), ③ z = 250 mm ($-45°$ roll) and ④ z = 400 mm ($135°$ roll). As schematized in Fig. 9, it is located on a PMMA supporting mast (dielectric constant $\epsilon_r = 2.65$, height: 992 mm, diameter: 40 mm). RCS measurements are made in HH polarization.

The RCS map is computed on a grid with $N \approx 1.7 \cdot 10^7$ voxels ($N_x \times N_y \times N_z = 256 \times 256 \times 256$). A spatial support constraint is defined around and behind the object as illustrated in Fig. 10. In Fig. 11, the SPRITE is compared to the conventional PFA and to ℓ_1 norm regularization method [13], [15]–[17]. The regularization parameters are manually tuned: $\mu = 5, \lambda = 10, \nu = 100$. The convergence time is 6 min 16 sec.

The resolution is drastically increased with the SPRITE of Fig. 11(c), in comparison to the PFA map Fig. 11(a). The main scatterers are perfectly located. As illustrated in Fig. 9, they come from the diffraction with the tip ①, each metallic patch ②, ③ and ④ and the rear edge ⑤. Behind the object, the SPRITE exhibits a scatterer ⑥ located at a distance of 87.6 mm from the cone base and that does not appear with the conventional method. After investigations, including RCS computations with a harmonic Maxwell solver [50], this scatterer turns out to originate from the interaction between the creeping wave and the supporting mast. Its location can be explained by the propagation delay inside the PMMA. Moreover, it can be noticed that with the ℓ_1 penalization method of Fig. 11(b), the map is only made up of scattering points. Conversely, the map obtained with the SPRITE is not only composed of scattering points but also of specular facets. It represents in a better way the physical reality of scattering mechanisms.

VI. Conclusion

A new high resolution approach has been proposed for 3-D radar imaging. The so-called SPRITE (SParse Radar Imaging TEchnique) takes into account in an original way the available prior knowledge on the wave-object interactions, extending the common point-wise scatterers to sparse facet-wise scatterers; it transcribes it into a ℓ_1-penalized high dimensional convex

non-differentiable criterion with possible support constraint. The radar map formation is achieved very efficiently by a suited Alternating Direction Method of Multipliers (ADMM) optimization algorithm, where the updates of the auxililary variables are direct and separable while the map update is computed very efficiently in the frequency domain by 3-D FFT and IFFT.

The SPRITE is evaluated on synthetic and real data. In comparison to the conventional method, the resolution is drastically enhanced. The main scatterers are recovered with increased accuracy, leading to a deeper understanding of the target scattering behavior and finally to a better RCS analysis and control. Unlike other recent ℓ_1 based methods, the SPRITE allows to reconstruct specular facets leading to a better wave-object interactions representation.

To go further, it would be interesting to move towards an unsupervised reconstruction that would automatically tuned the regularization parameters. Our conviction is that it could be worthwhile to adopt a Bayesian framework [28, chap. 8], [51]. Another perspective could be to take advantage of the informative sparse prior for compressed sensing [52], [53], i.e. to strongly reduce the required number of measurements while preserving the image quality. Finally, it could be interesting to conjointly estimate both the support and the map by using inversion/segmentation methods for instance [54], [55].

APPENDIX

A. Proof of Direct Matrix Model

Let us start again from the data collection. After a regridding phase, the acquisitions are placed on a k-space Cartesian grid in the k-space, with M_x points (resp. M_y and M_z) along the $\hat{\boldsymbol{k}}_x$-axis (resp. $\hat{\boldsymbol{k}}_y$-axis and $\hat{\boldsymbol{k}}_z$-axis). Note that, thanks to this regridding phase in the k-space and to the discretization of the spatial scattering distribution into a Cartesian grid, it is possible to perform computations efficiently with FFT and IFFT. Let us note the wave vector $\boldsymbol{k}_{m_x m_y m_z}$ ($m_\star = 0 \cdots M_\star - 1$ with $\star = x$, $\star = y$ and $\star = z$) in the k-space:

$$\boldsymbol{k}_{m_x m_y m_z} = k_x^{[m_x]} \hat{\boldsymbol{x}} + k_y^{[m_y]} \hat{\boldsymbol{y}} + k_z^{[m_z]} \hat{\boldsymbol{z}} \tag{13}$$

It is straightforward to show that the discretization of (2) leads to the corresponding complex scattering coefficient:

$$\sigma(\boldsymbol{k}_{m_x m_y m_z}) = \alpha \Psi_{m_x m_y m_z} \sum_{n_x=0}^{N_x-1} \sum_{n_y=0}^{N_y-1} \sum_{n_z=0}^{N_z-1} \left[a_{n_x,n_y,n_z} \Phi_{n_x n_y n_z} \, \mathrm{e}^{-\jmath\pi(\delta k_x \delta_x m_x n_x + \delta k_y \delta_y m_y n_y + \delta k_z \delta_z m_z n_z)} \right] \tag{14}$$

where the k-space sampling are $\delta k_x = \Delta k_x / M_x - 1$, $\delta k_y = \Delta k_y / M_y - 1$ and $\delta k_z = \Delta k_z / M_z - 1$ and with α, $\Psi_{m_x m_y m_z}$ and $\Phi_{n_x n_y n_z}$ given by:

$$\alpha = \mathrm{e}^{-2\jmath\pi(k_x^{[0]} x^{[0]} + k_y^{[0]} y^{[0]} + k_z^{[0]} z^{[0]})} \tag{15}$$

$$\Psi_{m_x m_y m_z} = \mathrm{e}^{-2\jmath\pi(x^{[0]} \delta k_x m_x + y^{[0]} \delta k_y m_y + z^{[0]} \delta k_z m_z)} \tag{16}$$

$$\Phi_{n_x n_y n_z} = \mathrm{e}^{-2\jmath\pi(k_x^{[0]} \delta_x n_x + \pi k_y^{[0]} \delta_y n_y + k_z^{[0]} \delta_z n_z)} \tag{17}$$

By definition, the Inverse Discrete Fourier Transform of the object of interest a is periodic in the spatial domain, among the three spatial directions. Besides, the k-space sampling conditions the field-of-view dimension in the spatial domain. Thus, if it does not totally include the object of interest, there is spatial aliasing [56], [57]. The Nyquist-Shannon theorem results in the limit conditions for avoiding aliasing: $\delta k_x \delta_x \leqslant 1/(N_x - 1)$, $\delta k_y \delta_y \leqslant 1/(N_y - 1)$ and $\delta k_z \delta_z \leqslant 1/(N_z - 1)$.

For given k-space sampling steps, in order to benefit from the largest spatial extensions and to reveal a 3-D Discrete Fourier Transform, we choose:

$$\delta k_x \delta_x = 1/N_x,\ \delta k_y \delta_y = 1/N_y,\ \delta k_z \delta_z = 1/N_z\,. \tag{18}$$

Consequently, (14) becomes:

$$\sigma(\boldsymbol{k}_{m_x m_y m_z}) = \alpha \Psi_{m_x m_y m_z} \sum_{n_x=0}^{N_x-1} \sum_{n_y=0}^{N_y-1} \sum_{n_z=0}^{N_z-1} \left[a_{n_x,n_y,n_z} \Phi_{n_x n_y n_z} \, \mathrm{e}^{-2\jmath\pi\left(\frac{m_x n_x}{N_x} + \frac{m_y n_y}{N_y} + \frac{m_z n_z}{N_z}\right)} \right] \tag{19}$$

that includes a 3-D Discrete Fourier Transform of the scattering object a.

Finally, the linear relation can be expressed by the direct model $\boldsymbol{\sigma} = \boldsymbol{H}\boldsymbol{a}$, where the matrix $\boldsymbol{H}$ is given by:

$$\boldsymbol{H} = \alpha\sqrt{N}\, \boldsymbol{\Delta}_\Psi \boldsymbol{S} \boldsymbol{F}_{3D} \boldsymbol{\Delta}_\Phi \tag{20}$$

with the following terms.

- α is the complex coefficient given by (15) and accounting for the origin phase difference of the spatial and the k-space grids.
- $N = N_x N_y N_z$ is the number of elements of vector $\boldsymbol{a}$, i.e. the number of voxels.
- $\boldsymbol{S}$ is the binary selection matrix that only selects the scattering coefficients associated to the k-space grid points previously assigned during the regridding phase.
- $\boldsymbol{F}_{3D} = \boldsymbol{F}_{N_x} \otimes \boldsymbol{F}_{N_y} \otimes \boldsymbol{F}_{N_z}$ is a 3-D DFT matrix and $\otimes$ symbolizes the Kronecker product.
- $\boldsymbol{\Delta}_\Psi$ is a diagonal matrix of phase difference in the k-space. The $(m_x m_y m_z)$-th element of the diagonal is $\Psi_{m_x m_y m_z}$ given by (16).
- $\boldsymbol{\Delta}_\Phi = \boldsymbol{\Delta}_{\Phi_y} \otimes \boldsymbol{\Delta}_{\Phi_x} \otimes \boldsymbol{\Delta}_{\Phi_z}$ is a diagonal matrix of phase difference in the spatial domain where:

$$\boldsymbol{\Delta}_{\Phi_x} = \mathrm{diag}\{\mathrm{e}^{-2\jmath\pi k_x^{[0]} \delta_x n_x},\ n_x = 0 \cdots N_x - 1\}$$

$$\boldsymbol{\Delta}_{\Phi_y} = \mathrm{diag}\{\mathrm{e}^{-2\jmath\pi k_y^{[0]} \delta_y n_y},\ n_y = 0 \cdots N_y - 1\}$$

$$\boldsymbol{\Delta}_{\Phi_z} = \mathrm{diag}\{\mathrm{e}^{-2\jmath\pi k_z^{[0]} \delta_z n_z},\ n_z = 0 \cdots N_z - 1\}.$$

B. Incomplete Nearest Neighbor Regridding Process

There is a vast literature devoted to 3-D regridding methods. Among them we can cite the trilinear interpolation and the nearest-neighbor interpolation (see [24] for details). In general, these methods consider each point of the Cartesian grid and

assigns to it an interpolation of neighboring acquisitions. The main disadvantage is that they basically complete the entire Cartesian grid, including unobserved spatial frequencies distant from the measured area. Conversely, the so-called *incomplete nearest neighbor* regridding process used in [58] and in this article, considers each acquisition and assign it to the closest point of the Cartesian grid. This approach has several features.

- It leaves "gaps" in the Cartesian grid, in particular for the locations distant from the acquisition grid.
- Several measurements can be assigned to the same point of the Cartesian grid and in this case they are averaged. This is a strict consequence of a rearrangement of the data fidelity term and this operation is accompanied by a modification of the variances of the errors. However, rigorous consideration of this modification would prohibit the implementation by FFT, so it is neglected.
- After the regridding process, the number of assigned points in the Cartesian grid is at most equal to the number of acquisitions. It limits the addition of untrue data.

Note that a part of the resolution improvement of the produced images also comes from the fact that our regridding method does not affect value where there is no measurement and does not force the unobserved coefficients to zero.

C. Proof of $\boldsymbol{a}-Update$

From (8), it is clear that $\mathcal{L}$ is a quadratic function of $\boldsymbol{a}$. Moreover, it is a real function of the complex variable $\boldsymbol{a}$ and by using the complex gradient definition given in [59, eq. (8.8)], we have:

$$\nabla_{\boldsymbol{a}}\mathcal{L}(\boldsymbol{a},\boldsymbol{v},\boldsymbol{u}) = \boldsymbol{G}\boldsymbol{a}-\boldsymbol{d}\,, \tag{21}$$

where the matrix $\boldsymbol{G}$ is given by:

$$\boldsymbol{G}=\boldsymbol{H}^{\dagger}\boldsymbol{H}+\rho_P\boldsymbol{P}^{\dagger}\boldsymbol{P}+\rho_D(\boldsymbol{D}_x^{\dagger}\boldsymbol{D}_x+\boldsymbol{D}_y^{\dagger}\boldsymbol{D}_y)+(\nu+\rho_{\mathcal{C}})\boldsymbol{I}_N$$

and the vector $\boldsymbol{d}$ reads:

$$\begin{aligned}\boldsymbol{d} = \boldsymbol{H}^{\dagger}\boldsymbol{\sigma} + \rho_P\boldsymbol{P}^{\dagger}(\boldsymbol{v}_P-\boldsymbol{u}_P) + \rho_D\big[\boldsymbol{D}_x^{\dagger}(\boldsymbol{v}_x-\boldsymbol{u}_x)\\ + \boldsymbol{D}_y^{\dagger}(\boldsymbol{v}_y-\boldsymbol{u}_y)\big] + \rho_{\mathcal{C}}(\boldsymbol{v}_{\mathcal{C}}-\boldsymbol{u}_{\mathcal{C}})\,.\end{aligned}$$

As the gradient (21) is an affine function of $\boldsymbol{a}$, the Hessian of (8) is constant and given by:

$$\nabla^2_{\boldsymbol{a}}\mathcal{L}(\boldsymbol{a},\boldsymbol{v},\boldsymbol{u}) = \boldsymbol{G}\,. \tag{22}$$

Moreover, it can be noticed that $\boldsymbol{G}$ is a Hermitian positive semi-definite matrix as a sum of Hermitian positive semi-definite matrices. Moreover, since $\nu \geqslant 0$ and $\rho_{\mathcal{C}} > 0$ the Hessian (22) is a (strict) positive definite matrix. It follows that (8) is a strictly convex quadratic function of $\boldsymbol{a}$.

From the SPRITE algorithm, the $\boldsymbol{a}$-*update* writes :

$$\boldsymbol{a}^{(k+1)} = \underset{\boldsymbol{a}}{\operatorname{argmin}}\,\mathcal{L}(\boldsymbol{a},\boldsymbol{v}^{(k)},\boldsymbol{u}^{(k)})$$

Hence, the unique minimizer $\boldsymbol{a}^{(k+1)}$ of $\mathcal{L}(\boldsymbol{a},\boldsymbol{v}^{(k)},\boldsymbol{u}^{(k)})$ is obtained by nullifying its gradient and yields:

$$\boldsymbol{a}^{(k+1)} = \boldsymbol{G}^{-1}\boldsymbol{d}^{(k)}$$

that can be computed by FFT, as given by (10).

D. Proof of $\boldsymbol{v}$-Updates

1) For the Updates of $\boldsymbol{v}_P$, $\boldsymbol{v}_x$ and $\boldsymbol{v}_y$: From the SPRITE algorithm, we have

$$\boldsymbol{v}_P^{(k+1)} = \underset{\boldsymbol{v}_P}{\operatorname{argmin}}\,\mathcal{L}(\boldsymbol{a}^{(k+1)},[\boldsymbol{v}_P\,\boldsymbol{v}_x^{(k)}\,\boldsymbol{v}_y^{(k)}\,\boldsymbol{v}_{\mathcal{C}}^{(k)}],\boldsymbol{u}^{(k)})$$

then by using (8) and from [46], it becomes:

$$\begin{aligned}\boldsymbol{v}_P^{(k+1)} &= \underset{\boldsymbol{v}_P}{\operatorname{argmin}}\Big\{\mu\|\boldsymbol{v}_P\|_1 + \frac{\rho_P}{2}\|\boldsymbol{P}\boldsymbol{a}^{(k+1)}-\boldsymbol{v}_P+\boldsymbol{u}_P^{(k)}\|_2^2\Big\}\\ &= \operatorname{prox}_{\mu\|\cdot\|_1/\rho_P}\big(\boldsymbol{P}\boldsymbol{a}^{(k+1)}+\boldsymbol{u}_P^{(k)}\big)\\ &= \mathrm{S}_{\mu/\rho_P}\Big(\boldsymbol{P}\boldsymbol{a}^{(k+1)}+\boldsymbol{u}_P^{(k)}\Big)\end{aligned}$$

where $\operatorname{prox}_{\mu\|\cdot\|_1/\rho_P}$ is the proximal operator of $\mu\|\cdot\|_1/\rho_P$ and S_{μ/ρ_P} the soft thresholding operator for complex variables.

A similar reasoning is applied for the $\boldsymbol{v}_x$ and $\boldsymbol{v}_y$ updates and provides the second part of (11).

2) For the $\boldsymbol{v}_{\mathcal{C}}$-Update: Let us consider the SPRITE algorithm and from (8), we have:

$$\begin{aligned}\boldsymbol{v}_{\mathcal{C}}^{(k+1)} &= \underset{\boldsymbol{v}_{\mathcal{C}}}{\operatorname{argmin}}\,\mathcal{L}(\boldsymbol{a}^{(k+1)},[\boldsymbol{v}_P^{(k+1)}\,\boldsymbol{v}_x^{(k+1)}\,\boldsymbol{v}_y^{(k+1)}\,\boldsymbol{v}_{\mathcal{C}}],\boldsymbol{u}^{(k)})\\ &= \underset{\boldsymbol{v}_{\mathcal{C}}}{\operatorname{argmin}}\Big\{\mathcal{I}_{\mathcal{C}}(\boldsymbol{v}_{\mathcal{C}}) + \frac{\rho_{\mathcal{C}}}{2}\|\boldsymbol{a}^{(k+1)}-\boldsymbol{v}_{\mathcal{C}}+\boldsymbol{u}_{\mathcal{C}}^{(k)}\|_2^2\Big\}\\ &= \operatorname{prox}_{\mathcal{I}_{\mathcal{C}}}\big(\boldsymbol{a}^{(k+1)}+\boldsymbol{u}_{\mathcal{C}}^{(k)}\big)\\ &= \mathcal{P}_{\mathcal{C}}(\boldsymbol{a}^{(k+1)}+\boldsymbol{u}_{\mathcal{C}}^{(k)})\end{aligned}$$

where $\operatorname{prox}_{\mathcal{I}_{\mathcal{C}}}$ is the proximal operator of the characteristic function $\mathcal{I}_{\mathcal{C}}$ of $\mathcal{C}$ and $\mathcal{P}_{\mathcal{C}}$ is the Euclidean projection onto $\mathcal{C}$.

REFERENCES

[1] D. L. Mensa, *High Resolution Radar Cross-Section Imaging*. Norwood, MA, USA: Artech House, 1981.

[2] J. Fortuny and A. Sieber, "Three-dimensional synthetic aperture radar imaging of a fir tree: First results," *IEEE Trans. Geosci. Remote Sens.*, vol. 37, no. 2, pp. 1006–1014, Mar. 1999.

[3] J. Tsao and B. Steinberg, "Reduction of sidelobe and speckle artifacts in microwave imaging: The CLEAN technique," *IEEE Trans. Antennas Propag.*, vol. 36, no. 4, pp. 543–556, Apr. 1988.

[4] M. Stuff, M. Biancalana, G. Arnold, and J. Garbarino, "Imaging moving objects in 3D from single aperture synthetic aperture radar," in *Proc. IEEE NRC*, 2004, pp. 94–98.

[5] R. Schmidt, "Multiple emitter location and signal parameter estimation," *IEEE Trans. Antennas Propag.*, vol. 34, no. 3, pp. 276–280, Mar. 1986.

[6] M. Burrows, "Two-dimensional ESPRIT with tracking for radar imaging and feature extraction," *IEEE Trans. Antennas Propag.*, vol. 52, no. 2, pp. 524–532, Feb. 2004.

[7] R. Roy, A. Paulraj, and T. Kailath, "ESPRIT - A subspace rotation approach to estimation of parameters of cisoids in noise," *IEEE Trans. Acoust., Speech, Signal Process.*, vol. 34, no. 5, pp. 1340–1342, Oct. 1986.

[8] G. Poulalion, S. Morvan, Y. Berthoumieu, and M. Najim, "A joint detection-estimation scheme for the analysis of noisy complex sinusoids," in *Proc. IEEE Int. Conf. Acoust., Speech Signal Process.*, 1997, vol. 5, pp. 3961–3964.

[9] R. Moch, T. Dallmann, and D. Heberling, "A tomographic approach to polarimetric RCS imaging," in *Proc. IEEE Eur. Conf. Antennas Propag.*, Mar. 2017, pp. 3940–3944.

[10] M. Bevacqua and T. Isernia, "Shape reconstruction via equivalence principles, constrained inverse source problems and sparsity promotion," *Progress Electromagn. Res.*, vol. 158, pp. 37–48, 2017.

[11] H. Aghababaee, G. Ferraioli, L. Ferro-Famil, G. Schirinzi, and Y. Huang, "Sparsity based full rank polarimetric reconstruction of coherence matrix T," *Remote Sens.*, vol. 11, no. 11, p. 1288, May 2019.

[12] M. Ambrosanio, P. Kosmas, and V. Pascazio, "A multithreshold iterative DBIM-based algorithm for the imaging of heterogeneous breast tissues," *IEEE Trans. Biomed. Eng.*, vol. 66, no. 2, pp. 509–520, Feb. 2019.

[13] M. Cetin, "Feature-enhanced synthetic aperture radar imaging," Ph.D. dissertation, Univ. College Eng., Boston, MA, USA, 2001.

[14] M. Herman and T. Strohmer, "High-resolution radar via compressed sensing," *IEEE Trans. Signal Process.*, vol. 57, no. 6, pp. 2275–2284, Jun. 2009.

[15] L. Potter, E. Ertin, J. Parker, and M. Cetin, "Sparsity and compressed sensing in radar imaging," *Proc. IEEE*, vol. 98, no. 6, pp. 1006–1020, Jun. 2010.

[16] C. Austin, E. Ertin, and R. Moses, "Sparse signal methods for 3D radar imaging," *IEEE J. Sel. Topics Signal Process.*, vol. 5, no. 3, pp. 408–423, Jun. 2011.

[17] B. Ji-Hoon, K. Byung-Soo, L. Seong-Hyeon, Y. Eunjung, and K. Kyung-Tae, "Bistatic ISAR image reconstruction using sparse-recovery interpolation of missing data," *IEEE Trans. Aerosp. Electron. Syst.*, vol. 52, no. 3, pp. 1155–1167, Jun. 2016.

[18] M. Lasserre, S. Bidon, and F. Le Chevalier, "New sparse-promoting prior for the estimation of a radar scene with weak and strong targets," *IEEE Trans. Signal Process.*, vol. 64, no. 17, pp. 4634–4643, Sep. 2016.

[19] X. Ren, L. Qiao, Y. Qin, and P. Li, "Sparse regularization based imaging method for inverse synthetic aperture radar," in *Proc. IEEE Progress Electromagn. Res. Symp.*, Aug. 2016, pp. 4348–4351.

[20] S. P. Boyd and L. Vandenberghe, *Convex Optimization*. Cambridge, U.K.: Cambridge Univ. Press, 2004.

[21] T. Benoudiba-Campanini, P. Minvielle, P. Massaloux, and J.-F. Giovannelli, "A new regularization method for radar cross section imaging," in *Proc. IEEE Eur. Conf. Antennas Propag.*, Mar. 2017, pp. 1419–1423.

[22] T. Benoudiba-Campanini, P. Minvielle, J.-F. Giovannelli, and P. Massaloux, "SPRITE : A new sparse approach for 3D high resolution RCS imaging," in *Proc. Int. Radar Conf.*, Mar. 2019, pp. 1–6.

[23] P. Minvielle, P. Massaloux, and J.-F. Giovannelli, "Indoor 3D radar imaging for low-RCS analysis," *IEEE Trans. Aerosp. Electron. Syst.*, vol. 53, no. 2, pp. 995–1008, Apr. 2017.

[24] C. Ozdemir, *Inverse Synthetic Aperture Radar Imaging With MATLAB Algorithms*. Hoboken, NJ, USA: Wiley, 2012.

[25] B. Borden, *Radar Imaging of Airborne Targets: A Primer for Applied Mathematicians and Physicists*. Bristol, Philadelphia: Institute of Physics, 1999.

[26] D. Hodge and F. Schultz, "The Born approximation applied to electromagnetic scattering from a finite cone," *Proc. IEEE*, vol. 53, no. 8, pp. 1066–1067, Aug. 1965.

[27] M. Cheney and B. Borden, *Fundamentals of Radar Imaging*. Philadelphia: Society for Industrial and Applied Mathematics, 2009.

[28] J. Idier, *Bayesian Approach to Inverse Problems*. Hoboken, NJ, USA: Wiley, 2008.

[29] J.-F. Giovannelli and J. Idier, *Regularization and Bayesian Methods for Inverse Problems in Signal and Image Processing*. Hoboken, NJ, USA: Wiley, 2015.

[30] P. Bühlmann and S. Van de Geer, *Statistics for High-Dimensional Data*. Berlin, Germany: Springer, 2011.

[31] E. Knott, J. Shaeffer, and M. Tuley, *Radar Cross Section*. 2nd Ed., Raleigh, NC: SciTech Pub, 2004.

[32] J.-F. Nouvel, A. Herique, W. Kofman, and A. Safaeinili, "Radar signal simulation: Surface modeling with the Facet method: Radar signal simulation," *Radio Sci.*, vol. 39, no. 1, pp. 1–17, Feb. 2004.

[33] B. R. Mahafza, *Radar Systems Analysis and Design Using MATLAB*. 3rd Ed. New York, NY, USA: Taylor & Francis, 2013.

[34] A. Chambolle, *An Algorithm for Total Variation Minimization and Applications.* vol. 20. Norwell, MA, USA: Kluwer, Jan. 2004 pp. 89–97.

[35] V. Olshevsky, I. Oseledets, and E. Tyrtyshnikov, "Tensor properties of multilevel Tœplitz and related matrices," *Linear Algebra Appl.*, vol. 412, no. 1, pp. 1–21, 2006.

[36] T. Benoudiba-Campanini, "Approche parcimonieuse pour l'imagerie 3D haute résolution de surface équivalente radar," Ph.D. dissertation, Univ. Bordeaux, Bordeaux, France, 2018.

[37] R. J. Tibshirani, "The LASSO problem and uniqueness," *Electron. J. Statist.*, vol. 7, pp. 1456–1490, 2013.

[38] D. Bertsekas, "Nondifferentiable optimization via approximation," in *Proc. Nondifferentiable Optim.*, 1975, vol. 3, pp. 1–25.

[39] B. T. Poliyak, *Introduction to Optimization*. New York: Optimization Software, Publications Division, 1987.

[40] P. Combettes and V. Wajs, "Signal recovery by proximal forward-backward splitting," *Multiscale Model. Simul.*, vol. 4, no. 4, pp. 1168–1200, Jan. 2005.

[41] P. L. Combettes and J.-C. Pesquet, "Proximal splitting methods in signal processing," in *Proc. Fixed-Point Algorithms Inverse Problems Sci. Eng.*, 2011, vol. 49, pp. 185–212.

[42] A. Beck and M. Teboulle, "Fast gradient-based algorithms for constrained total variation image denoising and deblurring problems," *IEEE Trans. Image Process.*, vol. 18, no. 11, pp. 2419–2434, Nov. 2009.

[43] J.-F. Giovannelli and A. Coulais, "Positive deconvolution for superimposed extended source and point sources," *Astronomy Astrophys.*, vol. 439, no. 1, pp. 401–412, Aug. 2005.

[44] M. V. Afonso, J. M. Bioucas-Dias, and M. A. T. Figueiredo, "An augmented Lagrangian approach to the constrained optimization formulation of imaging inverse problems," *IEEE Trans. Image Process.*, vol. 20, no. 3, pp. 681–695, Mar. 2011.

[45] S. Boyd, "Distributed optimization and statistical learning via the alternating direction method of multipliers," *Found. Trends Mach. Learn.*, vol. 3, no. 1, pp. 1–122, 2010.

[46] L. Li, X. Wang, and G. Wang, "Alternating direction method of multipliers for separable convex optimization of real functions in complex variables," *Math. Problems Eng.*, vol. 2015, pp. 1–14, 2015.

[47] B. R. Hunt, "The application of constrained least squares estimation to image restoration by digital computer," *IEEE Trans. Comput.*, vol. C-22, no. 9, pp. 805–812, Sep. 1973.

[48] H. C. Andrews and B. R. Hunt, *Digital Image Restoration*. Englewood Cliffs, NJ, USA: Prentice-Hall, Mar. 1977.

[49] B. Borden, "Maximum entropy regularization in inverse synthetic aperture radar imagery," *IEEE Trans. Signal Process.*, vol. 40, no. 4, pp. 969–973, Apr. 1992.

[50] B. Stupfel, R. Le Martrer, P. Bonnemason, and B. Scheurer, "Combined boundary-element and finite-element method for scattering problem by axi-symmetrical penetrable objects," *Math. Numer. Aspects Wave Propag. Phenomena*, vol. 1, pp. 332–341, 1991.

[51] F. Orieux, J.-F. Giovannelli, T. Rodet, and A. Abergel, "Estimating hyperparameters and instrument parameters in regularized inversion Illustration for *Herschel* /SPIRE map making," *Astronomy Astrophys.*, vol. 549, pp. 1–13, Jan. 2013.

[52] D. Donoho, "Compressed sensing," *IEEE Trans. Inf. Theory*, vol. 52, no. 4, pp. 1289–1306, Apr. 2006.

[53] E. Candes and M. Wakin, "An introduction to compressive sampling," *IEEE Signal Process. Mag.*, vol. 25, no. 2, pp. 21–30, Mar. 2008.

[54] C. Vacar and J.-F. Giovannelli, "Unsupervised joint deconvolution and segmentation method for textured images: A Bayesian approach and an advanced sampling algorithm," *EURASIP J. Adv. Signal Process.*, vol. 1, pp. 1–17, 2019.

[55] H. Ayasso and A. Mohammad-Djafari, "Joint NDT image restoration and segmentation using Gauss Markov Potts prior models and variational Bayesian computation," *IEEE Trans. Image Process.*, vol. 19, no. 9, pp. 2265–2277, Sep. 2010.

[56] H. Nyquist, "Certain topics in telegraph transmission theory," *Trans. Amer. Inst. Elect. Eng.*, vol. 47, no. 2, pp. 617–644, Apr. 1928.

[57] C. Shannon, "Communication in the presence of noise," *Proc. IRE*, vol. 37, no. 1, pp. 10–21, Jan. 1949.

[58] R. Boubertakh, J.-F. Giovannelli, A. Herment, and A. De Cesare, "Non-quadratic convex regularized reconstruction of MR images from spiral acquisitions," *Signal Process.*, vol. 86, pp. 2479–2494, 2006.

[59] S. Haykin, *Adaptive Filter Theory*. 3rd Ed. Englewood Cliffs, NJ, USA: Prentice-Hall, 1996.